Published in final edited form as:
*Nano Lett*. 2012 March 14; 12(3): 1176–1183. doi:10.1021/nl2031663.

# M13 phage-functionalized single-walled carbon nanotubes as nanoprobes for second near-infrared window fluorescence imaging of targeted tumors

**HYUNJUNG YI**[#1,2], **DEBADYUTI GHOSH**[#1,2], **MOON-HO HAM**[3], **JIFA QI**[1,2], **PAUL W. BARONE**[3], **MICHAEL S. STRANO**[3], and **ANGELA M. BELCHER**[1,2,4,*]

[1]Department of Materials Science and Engineering, Massachusetts Institute of Technology, Cambridge, Massachusetts 02139, USA

[2]David H. Koch Institute for Integrative Cancer Research, Massachusetts Institute of Technology, Cambridge, Massachusetts 02139, USA

[3]Department of Chemical Engineering, Massachusetts Institute of Technology, Cambridge, Massachusetts 02139, USA

[4]Department of Biological Engineering, Massachusetts Institute of Technology, Cambridge, Massachusetts 02139, USA

[#] These authors contributed equally to this work.

## Abstract

Second near-infrared (NIR) window light (950-1,400 nm) is attractive for *in vivo* fluorescence imaging due to its deep penetration depth in tissues and low tissue autofluorescence. Here we show genetically engineered multifunctional M13 phage can assemble fluorescent single-walled carbon nanotubes (SWNTs) and ligands for targeted fluorescence imaging of tumors. M13-SWNT probe is detectable in deep tissues even at a low dosage of 2 μg/mL and up to 2.5 cm in tissue-like phantoms. Moreover, targeted probes show specific and up to four-fold improved uptake in prostate specific membrane antigen positive prostate tumors compared to control non-targeted probes. This M13 phage-based second NIR window fluorescence imaging probe has great potential for specific detection and therapy monitoring of hard-to-detect areas.

### Keywords

Second near-infrared window fluorescence; single-walled carbon nanotubes; molecular imaging; hybrid imaging probes; nanobiotechnology

Fluorescence imaging is a powerful imaging modality for non-invasive and non-radiative detection of diseases and monitoring of treatment response[1]. Second near-infrared (NIR) window light (950-1,400 nm) is attractive for *in vivo* fluorescence imaging due to its greater penetration depth in tissues and low tissue autofluorescence compared to first NIR window light (650-950 nm)[2]. Single-walled carbon nanotubes (SWNTs) show great promise as *in vivo* fluorescence imaging agents due to their photoluminescence (PL) in the second NIR window and their interband transitions in the first NIR window (650 −950 nm) allowing for

[*]To whom correspondence should be addressed: belcher@mit.edu.

**Supporting Information Available**: materials, detailed experimental methods, and figures. This material is available free of charge via the Internet at http://pubs.acs.org

excitation far from the emission line, further reducing background coming from excitation. SWNTs have previously been used for fluorescence imaging of live cells *in vitro*[3] and whole animal *in vivo*[4, 5]. However, actively targeted, fluorescence imaging *in vivo* has not been achieved. This is because it is challenging to achieve stable, biocompatible, and bright SWNTs with sufficient intensity for *in vivo* second NIR window fluorescence imaging due to the extremely hydrophobic surface of SWNTs and the sensitivity of the fluorescence to defect creation and bundle formation. For successful *in vivo* fluorescence imaging, the fluorescence intensity of SWNTs is critical as recently shown using SWNTs prepared by surfactant exchange with biocompatible phospholipid-polyethylene glycol (PLPEG)[5]. Moreover, to further utilize the second NIR window fluorescence imaging for specific, accurate detection of targets such as malignant tumors and minimize non-specific uptake[6], coupling targeting functionality to brightly fluorescent SWNTs is required. However, there has been no report on method or material system to obtain targeted SWNTs with bright enough fluorescence for *in vivo* imaging.

M13 bacteriophage (or phage) is a versatile scaffold with five capsid proteins that can display material-specific peptides[7, 8] and/or targeting motifs[9] through genetic engineering. In addition, its filamentous shape (length ~880 nm and diameter ~6.5 nm) allows for multivalent interaction with one-dimensional materials such as SWNTs along the length of the phage, resulting in stable complexes (Fig. 1a). Recently, our group has shown that M13 phage with pH sensitive SWNT-binding peptide expressed on the major coat proteins, p8, can effectively stabilize SWNTs in aqueous solution and be utilized for highly efficient electron collection in photovoltaic devices[10]. However, the possibility of SWNTs stabilized by M13 phage (designated as M13-SWNT) for biological applications has never been reported, and the capability to genetically control the multiple capsid proteins of M13 and spatially segregate their functionalities could be advantageous for constructing targeted and fluorescent imaging probe complexes which have been challenging to realize.

In this report, we show that SWNTs stabilized by genetically engineered M13 phage can be successfully utilized as an efficient *in vivo* fluorescence imaging probe. Moreover, we demonstrate that genetically modified, multifunctional M13 phage can successfully incorporate targeting functionality into brightly fluorescent SWNTs for second NIR window fluorescence imaging of specific tumors *in vivo*. The M13-SWNT probe is detectable in deep tissues even at a low dosage of 2 μg/mL and up to 2.5 cm in tissue-like phantoms. In addition, antibody-targeted M13-SWNT probes show specific and up to four-fold improved uptake in prostate specific membrane antigen (PSMA) positive prostate tumors compared to control non-targeted probes. These results highlight the potential of the probe for specific detection and therapy monitoring of hard-to-detect areas.

To assess M13-SWNT as an efficient fluorescence imaging agent, optical properties and fluorescence stability of M13-SWNTs prepared as previously described[10] were first investigated. In this study, SWNTs prepared by high-pressure carbon monoxide (HiPCO) were chosen rather than fluorescent semiconductor-rich CoMoCAT SWNTs since HiPCO SWNTs have more SWNT species with relatively large diameters which fluoresce at longer wavelengths (up to ~1,600 nm) than CoMoCAT SWNTs (up to ~1,100 nm)[10]. The absorption spectrum and PL excitaion (PLE) map of the M13-SWNT probe in phosphate-buffered saline (PBS) was compared to SWNTs dispersed by 2wt% sodium cholate (SC) in distilled water, denoted as SC-SWNTs (Fig. 1b and 1c). The optical transition peaks of M13-SWNTs show a small red shifting, most obvious in the lowest-energy interband transition (wavelengths > 900 nm). The red shifting is due to different dielectric environments surrounding the SWNTs after surfactant exchange with the M13 phage[11], and small bundling of SWNTs during the complexation[10]. The relative quantum yield of M13-SWNT probe, calculated by comparing integrated PL intensity (957 nm- 1,291 nm), is about

40% of the starting SC-SWNTs, and this relative quantum yield of M13-SWNTs is sufficient for *in vivo* imaging as shown later (Fig. 2a and Fig. 4a). To test fluorescence stability, the M13-SWNT probe in PBS was mixed with equal volume of either 100% fetal bovine serum (FBS) or cell culture media supplemented with 10% FBS, and NIR PL intensities of solutions were measured at various time points up to 24 h after mixing (Fig. 1d). M13-SWNTs in PBS and the culture media with 10% FBS retained their integrated PL intensity throughout the tested period, while the probe in FBS showed a slight decrease in the PL intensity after 3 h incubation. The decrease of PL intensity could be attributed to the adsorption of serum proteins on the sidewall of SWNTs[12] because the surface of SWNTs bound by M13 is partially exposed to the solution[10]. However, the PL intensity remained around 90% after the initial decrease and did not show noticeable aggregation, indicating the probe is very stable[13]. Therefore, these genetically engineered M13-stabilized fluorescence probes are serum stable and brightly fluorescent, showing promise for *in vivo* imaging.

We next examined the potential of the M13-SWNT probe for *in vivo* fluorescence imaging using a custom-built NIR imager (Supplementary Fig. S1). Mice were imaged from the dorsal side before and after intravenous injection (Fig. 2a) with 200 μL of 30 μg/mL of SWNTs. Before injection, there is negligible tissue autofluorescence, which is one of the advantages of second NIR window fluorescence imaging. At 10 min post-injection (p.i.), fluorescent M13-SWNTs are visualized throughout the vasculature and are evident in the highly fenestrated, vascular-rich kidneys. This vasculature is still visible but less obvious at 1 h p.i. and becomes featureless at 4 h p.i.., consistent with the observed blood circulation behavior (Fig. 2b). The kinetics of M13-SWNT is beneficial for imaging since the ability to optimize tissue uptake while minimizing the background signal from circulation is critical towards successful imaging[14]. Fluorescence from M13-SWNT probe is mostly observed in liver, spleen, and bone due to immune clearance by these organs of the reticuloendothelial system. Similar clearance has been reported with other nanomaterials[15] including SWNTs[16] and quantum dot (>20 nm) probes[17]. It is noted that raw signal from liver and spleen is clearly detected from the dorsal side, which is challenging to obtain using visible or first NIR window light. We could detect M13-SWNT probes in deep organs even at a low dosage of 2 μg/ml of SWNTs (0.022 mg/kg) (Fig. 2c) and up to 2.5 cm depth in tissue-like phantoms (Fig. 2d and Supporting Information). These low dosage and depth results highlight the advantages of the second NIR window fluorescent M13-SWNT probe.

Taking advantage of the versatility of the M13 scaffold, various targeting moieties were then incorporated into M13 and further screened for efficient targeting *in vitro*. To couple targeting functionality to SWNTs without compromising the fluorescence of SWNTs, minor coat protein p3, located at the proximal tip of M13 and spatially separated from SWNT-binding p8 proteins, was engineered to express either peptide ligands or peptide handles for site-specific antibody conjugation (Fig. 1a and Supporting Information). A peptide identified from phage display against Secreted Protein, Acidic and Rich in Cysteine (SPARC) (SPARC-binding peptide, designated as SBP)[18] was genetically engineered into the p3 protein of the SWNT binding M13. SPARC is a matricellular protein overexpressed in various cancers, including prostate, breast and skin (reviewed in reference [19]). For an antibody binding system, we engineered a 15-amino acid biotin acceptor peptide (BAP) tag[20] onto the p3 of M13 for site-specific conjugation of antibodies (Supporting Information). The resulting BAP expressing M13 was biotinylated using *birA* biotin protein ligase enzyme in appropriate buffer conditions at 30°C for 12 h. After the reaction, the biotinylated phage was purified by standard PEG/NaCl precipitation method. The enzymatically biotinylated peptide allows us to add any streptavidin-conjugated antibodies for desired targeting and removes the need for more complex and non-specific conjugation chemistries. Here we conjugated an antibody against the extracellular domain of prostate specific membrane antigen (PSMA), a cell surface marker overexpressed in various prostate

carcinomas and endothelium of tumor vasculature[21, 22]. To conjugate PSMA antibody to p3, approximately 500 μL of biotinylated phage-SWNT complex solution at $3 \times 10^{13}$ complexes/mL was incubated with 10 μL of streptavidin-conjugated antibody at room temperature for 12 h.

For screening, M13-SWNT probes displaying SPARC-binding peptide, PSMA antibody, or no ligand (denoted as SBP-M13-SWNT, anti-PSMA-M13-SWNT, and M13-SWNT, respectively) were incubated on LNCaP (higher SPARC expression and PSMA positive) and DU145 (low SPARC expression and PSMA negative) human prostate cancer cell lines and NIR fluorescence was measured to quantify specific uptake. There is about 5.3-fold and 8.3-fold enhanced uptake of SBP-M13-SWNT and anti-PSMA-M13-SWNT in LNCaP compared to DU145, respectively (Fig 3a). In the control, there is only minimal background fluorescence present in DU145 and LNCaP and no targeting was observed. These results correlate with the expression level of PSMA and SPARC (Fig. 3b). Flow cytometry (Supporting Information) confirms PSMA expression in LNCaP, whereas DU145 is negative for PSMA (Fig. 3b, top row). Moreover, there is moderate SPARC expression in LNCaP compared to DU145 control (Fig. 3b, bottom row). Interestingly, there is approximately 3.9-fold improvement in LNCaP targeting using anti-PSMA-M13-SWNT compared to SBP-M13-SWNT (Fig. 3a). This could be explained by the difference in the expression of cell surface markers, as confirmed by flow analysis. However, it is also possible that the different binding affinity of peptide versus antibodies may affect uptake[23]. By testing target and control cell lines, this *in vitro* assay allows us to screen probes and validate uptake and specificity of our probes.

Based on *in vitro* screening, we identified anti-PSMA-M13-SWNT as our best targeting candidate probe for subsequent investigation of tumor targeting and imaging *in vivo*. For the study of targeted imaging *in vivo*, human xenograft prostate tumors were induced in six-to-eight week old male nude *nu/nu* mice. Mice were subcutaneously injected in the right flank with $3 \times 10^6 – 4 \times 10^6$ LNCaP cells suspended with equal volume of Matrigel. Tumors were grown until they reached 3-7 mm in diameter. Upon formation of tumors, mice were injected intravenously with 200 μL of 30 μg/mL anti-PSMA-M13-SWNT and no targeting ligand control M13-SWNT and imaged at several intervals up to 24 h p.i. The fluorescence signal from anti-PSMA-M13-SWNT targeted tumor is clearly observed after 2 h and 4 h p.i. (Fig. 4a, indicated with white arrows) and reaches a maximum of ~200% increase in PL intensity at 4 h p.i. (Fig. 4a, right column and Fig. 4b). However, no obvious fluorescence image of tumor is observed when injected with control M13-SWNT probe (Fig. 4a, left column). Here, all the fluorescence images shown in fig. 4a are unprocessed, background-only subtracted images. The tumor accumulation kinetics of anti-PSMA-M13-SWNT is compared to the control M13-SWNT by quantifying the regions of interest from the collected fluorescent images at different timepoints (Fig. 4b). At 4 h p.i., mice injected with anti-PSMA-M13-SWNT show four-fold improved relative tumor PL increase compared to control M13-SWNT, indicating targeted uptake. At this timepoint, the probe has already cleared circulation and has accumulated in tumors. Tumors injected with negative control M13-SWNT probe have an initial increase upon intravenous injection, but decrease and reach background levels, suggesting minimal accumulation (Fig. 4b). Interestingly, at 1 h p.i., both tumored mice show similar levels of PL increase (Figs. 4a and 4b) due to circulating probes (Fig. 2b), making it difficult to specifically discern tumors at the earlier timepoints. The targeted accumulation of anti-PSMA-M13-SWNT compared to no ligand control M13-SWNT shown in Fig. 4a is further confirmed using image processing as presented in Fig. 4c. For image processing, fluorescence images collected at 1 h p.i. were subtracted from those at 4 h p.i. (Fig. 4a) after aligning the mouse positions using an image gradient based rigid registration[24] to remove effects from translation and rotation of the mouse, followed with a deformable image registration[25] to compensate for small

deformations in limb positions and changes caused by breathing cycle, and the change of PL intensity is represented as scaled colors (Fig. 4c). The positive number (red-side) indicates the increase of PL intensity and the negative value (blue-side) represents a decrease of PL intensity. The increase of PL intensity around tumor is clearly seen in the anti-PSMA-M13-SWNT-injected mouse whereas there is no obvious PL increase around tumor in the non-targeting probe-injected mouse, indicating the selective accumulation of probe in the targeting tumors. It is noted that in addition to the tumor, there are other areas showing PL intensity changes and these changes are mainly due to the misalignment while registering the two mouse positions.

After 4 h, there is a decrease of anti-PSMA-M13-SWNT accumulation in tumors (Figs. 4a, right and 4b), and this behavior may be mediated by M13 phage. Similar kinetics of targeted phage accumulation in tumors have been reported by others[18]. Probes targeting molecules overexpressed in tumor vasculature can exit, leading to decreased tumor accumulation at later time points. Since M13 is a large macromolecule (> 200 nm) and less likely to penetrate the vascular wall compared to small drugs or peptides[23], it likely targets PSMA also overexpressed in the tumor vasculature[22]. It is feasible that the decrease of PL intensity observed in both non-targeted and targeted probes may be partially due to the possible degradation of M13 phage by metabolic activity of cells and tissues, leading to bundling of SWNTs and quenching of their fluorescence. However, this behavior would occur with both non-targeted and targeted probes and therefore the PL difference between probes can still be attributed to targeted uptake.

To further confirm targeting, probe uptake in tumors was analyzed *ex vivo*. To quantify tumor uptake relative to muscle background, fluorescent images of the tumor and muscle excised at 24 hr p.i. were acquired and fluorescent intensities of image regions of interest were obtained. The NIR PL ratio of tumor to muscle of anti-PSMA-M13-SWNT is ~2.9 and this ratio is about two fold higher than non-targeted M13-SWNT (~1.4) (Fig. 5a), indicating preferential tumor uptake of anti-PSMA-M13-SWNT. We also confirmed anti-PSMA-M13-SWNT uptake at the microscale by NIR fluorescent microscopy. Harvested tissues and tumors were embedded in OCT resin and snap frozen in dry ice, and then cut into five micron sections. NIR fluorescence microscopy of sectioned tumors confirms anti-PSMA-M13-SWNT accumulation (Fig. 5b, upper right panel), whereas M13-SWNT is not seen in tumors (Fig. 5b, upper left panel). To validate uptake is specific and selective, PSMA expression on both tumors were examined through immunostaining. Adjacent tumor sections were probed with anti-PSMA antibody and secondary horseradish peroxidase conjugate and incubated with DAB chromogenic substrate. The resulting brown color of tumor sections (Fig. 5b, bottom row) is indicative of PSMA expression in both tumors, confirming uptake of anti-PSMA-M13-SWNT is specific and not artifactual.

It is noted that the two-fold improvement in PSMA targeting *in vivo* achieved in this work is equivalent to results reported by others targeting PSMA using aptamers and antibodies with diblock polymers[26], quantum dots[27], and indocyanine green conjugates[28]. Increasing targeting efficiency of nanoparticles is a challenge to the nanomedicine community. To improve targeting of the phage-based nanoprobes, other combinations of targeting ligands/antibodies and receptors could be exploited. Moreover, the phage targeting platform can be combined with methods to further amplify tumor targeting, including bioorthogonal chemistries[29] for pre-targeting, biomimetic amplification[30], and communicating nanoparticles[31].

In addition to enabling targeted fluorescence imaging of tumors in the longer wavelength window (beyond 1000 nm), the phage-based probe could offer other unique opportunities. First, due to the filamentous structure and genetically modifiable various capsid proteins of

M13, multiple imaging nanoparticles or SWNTs can be loaded along the phage and targeting ligands can be conjugated onto the tip of the phage site-specifically, enabling delivery of a higher payload of nanoparticles to receptors, thereby enhancing detection sensitivity. This configuration is difficult to achieve with other nanoparticle-based imaging schemes and this scheme will be particularly useful when the target receptor density of the tumor cells is low. Second, since there are more functional groups for further modification on major coat protein, p8, and the other tip protein, p9, of the phage, different nanoparticles such as gold nanorods[32] or iron oxides[33] can be easily conjugated onto the phage for enhanced fluorescence or multimodality imaging.

Using genetically modified multifunctional M13 phage as a template to assemble fluorescent single-walled carbon nanotubes (SWNTs) and ligands, we have successfully utilized SWNTs for second NIR window fluorescence imaging of molecularly targeted tumors for the first time. By engineering multiple capsid proteins of M13 phage independently, we were able to incorporate targeting capability into SWNTs without compromising the *in vivo* stability of the fluorescence of SWNTs. M13-SWNT probe was detectable in deep tissues even at a low dosage (2 μg/mL) and up to 2.5 cm in tissue-like phantoms, showing the potential for early, non-invasive diagnosis and clinical procedures, such as intra-operative surgery[13, 34, 35].

Future work to develop image processing methods[36] and enhance signal amplification of M13-SWNT through utilizing longer SWNTs[37], additional genetic engineering of the M13 phage for multiple peptide display[38], and synthesizing hybrid materials for metal enhanced fluorescence of SWNTs[32], and further amplify tumor targeting utilizing bioorthogonal chemistries[29] for pre-targeting, biomimetic amplification[30], and communicating nanoparticles[31] will allow us to image traditionally hard-to-detect areas.

## Supplementary Material

Refer to Web version on PubMed Central for supplementary material.

## Acknowledgments

Support for this work was partially funded from the National Cancer Institute Center for Cancer Nanotechnology Excellence (U54-CA119349-04). Construction of the imager was supported by a generous gift by the Marble family. H. Y. is grateful for the Korean Government Overseas Scholarship. We thank Dr. Lily Lee for the imaging processing and helpful discussions. We would like to acknowledge Denise Crowley and Michael Brown from the Histology Core of the Koch Institute (KI) Swanson Biotechnology Center for excellent assistance with immunohistochemical staining. We would like to thank Scott Malstrom from the Applied Therapeutics and Whole Animal Imaging Core of the KI Swanson Biotechnology Center with help regarding imaging. We would also like to thank Neel Bardhan for helpful discussions.

## References

1. Weissleder R, Pittet M. Nature. 2008; 452(7187):580–589. [PubMed: 18385732]
2. Smith AM, Mancini MC, Nie S. Nat Nanotechnol. 2009; 4(11):710–1. [PubMed: 19898521]
3. Welsher K, Liu Z, Daranciang D, Dai H. Nano Lett. 2008; 8(2):586–90. [PubMed: 18197719]
4. Leeuw TK, Reith RM, Simonette RA, Harden ME, Cherukuri P, Tsyboulski DA, Beckingham KM, Weisman RB. Nano Lett. 2007; 7(9):2650–4. [PubMed: 17696559]
5. Welsher K, Liu Z, Sherlock SP, Robinson JT, Chen Z, Daranciang D, Dai H. Nat Nanotechnol. 2009; 4(11):773–80. [PubMed: 19893526]
6. He X, Gao J, Gambhir SS, Cheng Z. Trends Mol Med. 2010; 16(12):574–83. [PubMed: 20870460]
7. Huang Y, Chiang CY, Lee SK, Gao Y, Hu EL, De Yoreo J, Belcher AM. Nano Letters. 2005; 5(7): 1429–1434. [PubMed: 16178252]

8. Lee YJ, Yi H, Kim WJ, Kang K, Yun DS, Strano MS, Ceder G, Belcher AM. Science. 2009; 324(5930):1051–1055. [PubMed: 19342549]
9. Cwirla SE, Peters EA, Barrett RW, Dower WJ. Proc Natl Acad Sci U S A. 1990; 87(16):6378–82. [PubMed: 2201029]
10. Dang X, Yi H, Ham MH, Qi J, Yun DS, Ladewski R, Strano MS, Hammond PT, Belcher AM. Nat Nanotechnol. 2011
11. Choi JH, Strano MS. Applied Physics Letters. 2007; 90(22):223114.
12. Cherukuri P, Gannon CJ, Leeuw TK, Schmidt HK, Smalley RE, Curley SA, Weisman RB. Proc Natl Acad Sci U S A. 2006; 103(50):18882–6. [PubMed: 17135351]
13. Kim S, Lim YT, Soltesz EG, De Grand AM, Lee J, Nakayama A, Parker JA, Mihaljevic T, Laurence RG, Dor DM, Cohn LH, Bawendi MG, Frangioni JV. Nat Biotechnol. 2004; 22(1):93–7. [PubMed: 14661026]
14. Weissleder R. Science's STKE. 2006; 312(5777):1168.
15. Longmire M, Choyke PL, Kobayashi H. Nanomedicine (Lond). 2008; 3(5):703–17. [PubMed: 18817471]
16. Liu Z, Davis C, Cai W, He L, Chen X, Dai H. Proc Natl Acad Sci U S A. 2008; 105(5):1410–5. [PubMed: 18230737]
17. Cai W, Shin DW, Chen K, Gheysens O, Cao Q, Wang SX, Gambhir SS, Chen X. Nano Lett. 2006; 6(4):669–76. [PubMed: 16608262]
18. Kelly KA, Waterman P, Weissleder R. Neoplasia. 2006; 8(12):1011–1018. [PubMed: 17217618]
19. Clark CJ, Sage EH. J Cell Biochem. 2008; 104(3):721–32. [PubMed: 18253934]
20. Beckett D, Kovaleva E, Schatz PJ. Protein Sci. 1999; 8(4):921–9. [PubMed: 10211839]
21. Wright GL Jr. Haley C, Beckett ML, Schellhammer PF. Urol Oncol. 1995; 1(1):18–28. [PubMed: 21224086]
22. Liu H, Moy P, Kim S, Xia Y, Rajasekaran A, Navarro V, Knudsen B, Bander NH. Cancer Res. 1997; 57(17):3629–34. [PubMed: 9288760]
23. Ruoslahti E, Bhatia SN, Sailor MJ. Journal of Cell Biology. 2010; 188(6):759–768. [PubMed: 20231381]
24. Bergen, JR.; Anandan, P.; Hanna, KJ.; Hingorani, R. Hierarchical Model-Based Motion Estimation. Proceedings of the Second European Conference on Computer Vision; Springer-Verlag; 1992.
25. Sand, P.; Teller, S. Particle Video: Long-Range Motion Estimation using Point Trajectories, Computer Vision and Pattern Recognition, 2006 IEEE Computer Society Conference on, 2006; 2006; p. 2195-2202.
26. Gu F, Zhang L, Teply BA, Mann N, Wang A, Radovic-Moreno AF, Langer R, Farokhzad OC. Proc Natl Acad Sci U S A. 2008; 105(7):2586–91. [PubMed: 18272481]
27. Shi C, Zhu Y, Xie Z, Qian W, Hsieh CL, Nie S, Su Y, Zhau HE, Chung LW. Urology. 2009; 74(2): 446–51. [PubMed: 19428067]
28. Nakajima T, Mitsunaga M, Bander NH, Heston WD, Choyke PL, Kobayashi H. Bioconjug Chem. 2011; 22(8):1700–5. [PubMed: 21740058]
29. Devaraj NK, Weissleder R, Hilderbrand SA. Bioconjug Chem. 2008; 19(12):2297–9. [PubMed: 19053305]
30. Simberg D, Duza T, Park JH, Essler M, Pilch J, Zhang L, Derfus AM, Yang M, Hoffman RM, Bhatia S, Sailor MJ, Ruoslahti E. Proc Natl Acad Sci U S A. 2007; 104(3):932–6. [PubMed: 17215365]
31. von Maltzahn G, Park JH, Lin KY, Singh N, Schwoppe C, Mesters R, Berdel WE, Ruoslahti E, Sailor MJ, Bhatia SN. Nat Mater. 2011; 10(7):545–52. [PubMed: 21685903]
32. Hong G, Tabakman SM, Welsher K, Chen Z, Robinson JT, Wang H, Zhang B, Dai H. Angew Chem Int Ed Engl. 2011; 50(20):4644–8. [PubMed: 21506225]
33. Choi JH, Nguyen FT, Barone PW, Heller DA, Moll AE, Patel D, Boppart SA, Strano MS. Nano Lett. 2007; 7(4):861–7. [PubMed: 17335265]
34. Whitney MA, Crisp JL, Nguyen LT, Friedman B, Gross LA, Steinbach P, Tsien RY, Nguyen QT. Nat Biotechnol. 2011; 29(4):352–6. [PubMed: 21297616]

35. Nguyen QT, Olson ES, Aguilera TA, Jiang T, Scadeng M, Ellies LG, Tsien RY. Proceedings of the National Academy of Sciences of the United States of America. 2010; 107(9):4317–4322. [PubMed: 20160097]

36. Welsher K, Sherlock SP, Dai H. Proc Natl Acad Sci U S A. 2011

37. Rajan A, Strano MS, Heller DA, Hertel T, Schulten K. J Phys Chem B. 2008; 112(19):6211–3. [PubMed: 18327930]

38. Nam KT, Kim DW, Yoo PJ, Chiang CY, Meethong N, Hammond PT, Chiang YM, Belcher AM. Science. 2006; 312(5775):885–8. [PubMed: 16601154]

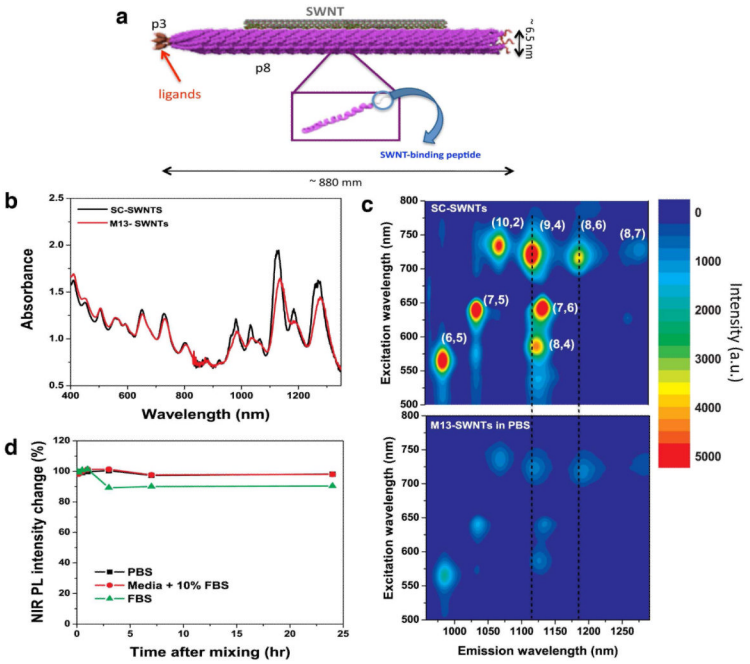


**Fig. 1. Schematic of the imaging probe and its characteristics**

**a**, M13-SWNT imaging probe: p8 is used to stably disperse SWNTs along the length of the virus, p3 is engineered for targeting with three different ligands, SPARC binding peptide (SBP), PSMA-antibody (anti-PSMA), and no-ligand. **b**, UV-vis-NIR absorption spectra and **c**, PL excitation (PLE) map of M13-SWNTs in phosphate-buffered saline (PBS) compared to SWNTs dispersed by 2wt% sodium cholate (SC) in distilled water (denoted as SC-SWNTs). There is small red shifting of peaks. **d**, Serum stability test of M13-SWNTs. M13-SWNT is incubated in PBS, fetal bovine serum (FBS) and tissue culture media with 10% FBS, and PL intensity is measured to 24 h. HiPCO SWNTs are used for all studies.

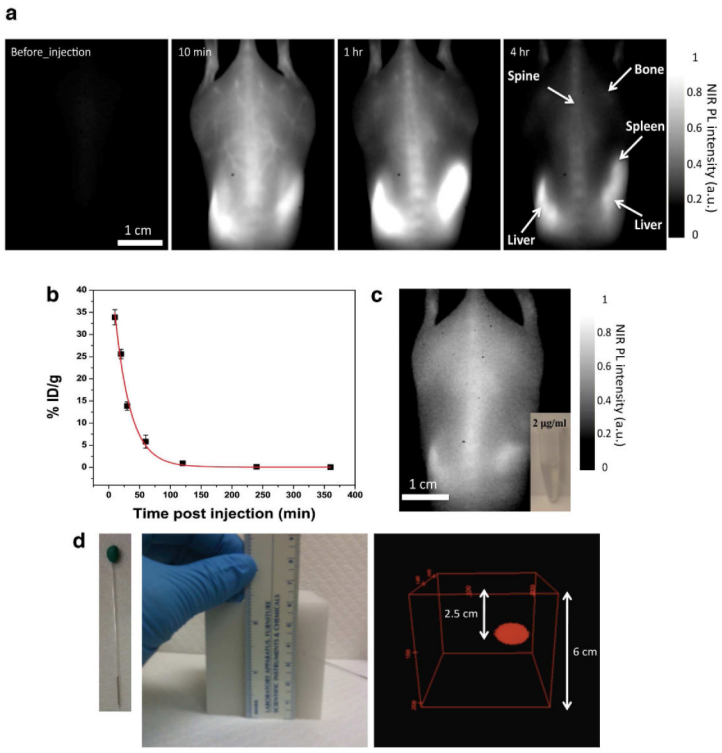


**Fig. 2. Kinetics and sensitivity of the fluorescent M13-SWNT imaging probe**

**a**, Fluorescence images of M13-SWNT injected mouse at various time points. At 10 min and 1 h post-injection (p.i.), vasculature and fenestrated kidneys can be observed. Dosage was 0.33 μg of SWNT/g (200 μL of 30 μg/mL SWNTs probe solution) and acquisition times for all images were 0.5 s. Signals from liver, spleen, bone, and spine are indicated by arrows. **b,** Blood circulation of M13-SWNT. The circulation time was determined as the timepoint when %ID/g of SWNT in blood falls to 5%, and the blood circulation of M13-SWNT was approximately 60 min. Each data point is the mean ± s.d. from n=3 animals. **c,** Fluorescence image of a mouse injected with 2 μg/mL (200 μL, 0.022 mg/kg of SWNTs) probe solution. Liver and spleen are clearly seen on the dorsal side. Image was taken at 2 h p.i. Acquisition time was 0.5 s. **d,** Penetration depth of M13-SWNT in tissue-like phantom studies. Quartz capillary tube of M13-SWNT (left) is inserted into 6 $cm^3$ tissue phantom (middle) and imaged using custom-built imager. Reconstructed 3D stacked image (right) shows M13-SWNT detectable at 2.5 cm depth.

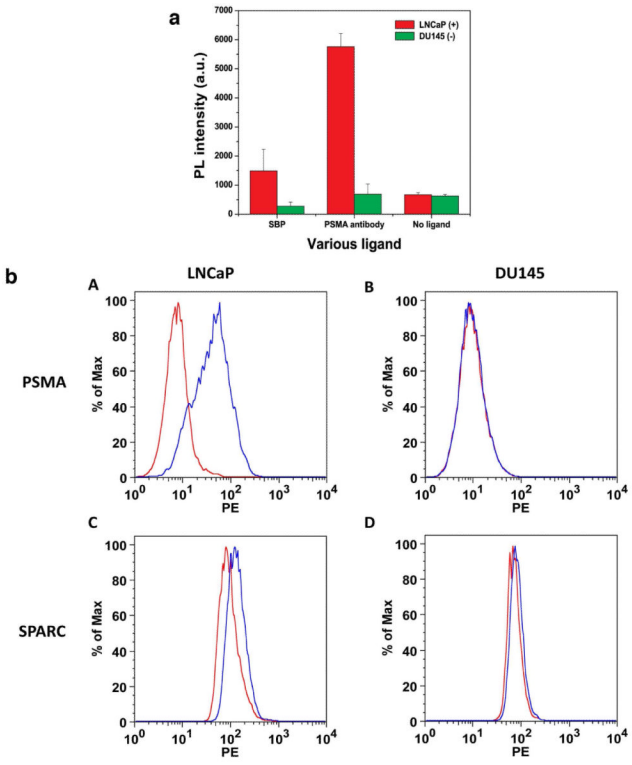


**Fig. 3. Targeting of the probe *in vitro***

**a**, *In vitro* binding assay of SBP, anti-PSMA, and no ligand displayed on the probe and incubated on LNCaP and DU145 prostate carcinoma cell lines. PL intensities are measured using custom-built imager. Acquisition times were 1 s for all samples. **b**, Expression of PSMA and SPARC in LNCaP and DU145 cell lines. FACS analysis shows expression of PSMA and SPARC in LNCaP (A, C blue histogram), respectively. Expression is not seen in DU145 cell line (B, D blue histogram). Red histogram is control.

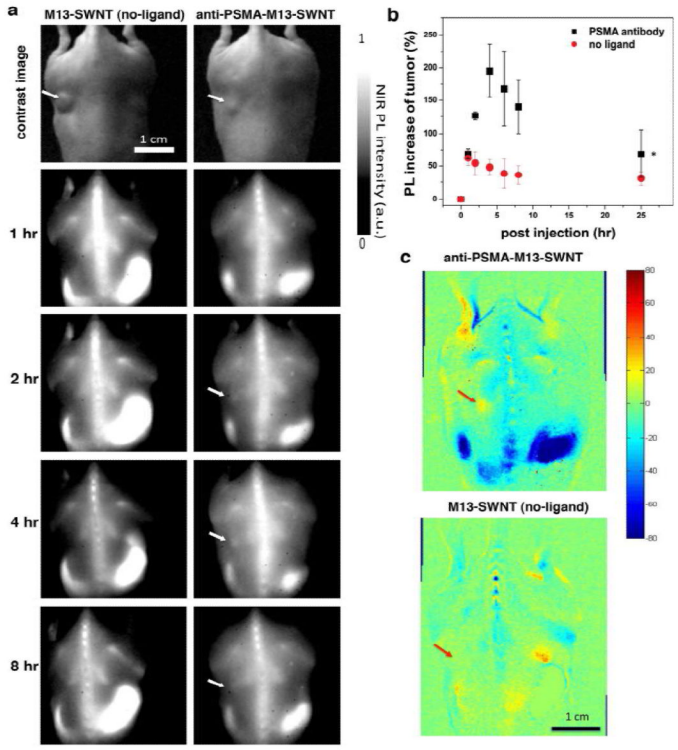


**Fig. 4. *In vivo* targeting of tumors**

**a**, *In vivo* second NIR window fluorescence images for LNCaP tumor-bearing mouse injected with anti-PSMA-M13-SWNT (right column) or control M13-SWNT (without ligand, left column) probes, taken at different time points. The clear tumor uptake of anti-PSMA-M13-SWNT injected mouse, maximized at 4 h p.i., shows active targeting capability of the probe. No obvious fluorescence image of tumors was observed throughout the timecourse when injected with control M13-SWNT (left column). Tumor areas are indicated by white arrows. All images are unprocessed, background-only subtracted. Acquisition times for the M13-SWNT mouse and the anti-PSMA-M13-SWNT mouse were 0.3 s and 0.5 s, respectively. **b**, Kinetics of tumor targeting. Each data point is the mean ± s.d. from n=3 animals. *P <0.01 for the entire set of data compared to no-ligand, using student *t-test* for paired data with one-tailed distribution. c. Processed images of tumor accumulation of anti-PSMA-M13-SWNT (top) and control M13-SWNT (bottom) probes. Images collected at 1 h p.i. were subtracted from those at 4 h p.i. (Fig. 4a) after applying a rigid image registration followed by a deformable image registration, and the change of PL intensity is represented as scaled colors (positive number in red indicates increase of PL intensity and the negative value in blue represents a decrease of PL intensity). PL intensity changes in other regions are attributed to the misalignment while registering the two mouse positions.

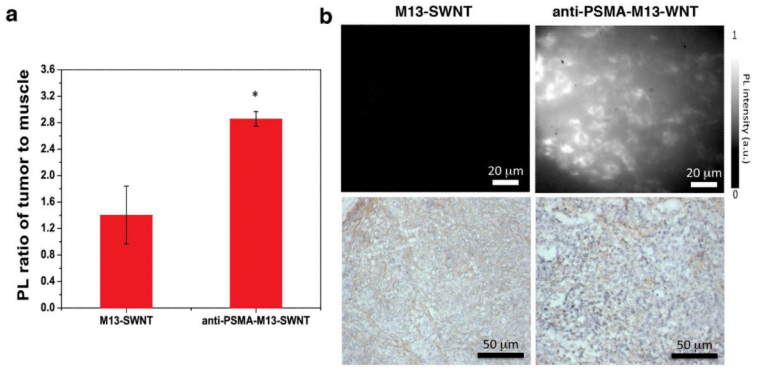


**Fig. 5. *Ex vivo* analysis of tumor targeting**

**a**, Relative targeted tumor uptake of anti-PSMA-M13-SWNT compared to no ligand control was determined from NIR PL intensity ratios of tumor to muscle. Tumors and muscles were collected at 24 h p.i.. Acquisition times for all samples were 0.5 s. Each data point is the mean ± s.d. from n=3 animals. *P <0.05 compared to no-ligand, using student *t-test* for paired data with one-tailed distribution. **b**, Probe uptake *in vivo* and immunohistochemistry (IHC) (lower row). LNCaP tumors were injected with anti-PSMA-M13-SWNT or M13-SWNT (without ligand) probe, shown in the right column and left column respectively. Five micron-cut serial sections were measured for SWNT fluorescence (upper row) and stained for PSMA expression (brown) (bottom row). PSMA expression in both tumors confirms anti-PSMA-M13-SWNT uptake (upper right panel) is specific and non-artifactual. The acquisition times for PL microscopy were 1 s and images for IHC were taken at 15 ms.